Measurement of *CP*-violation asymmetries in $D^0 \to K_S^0 \pi^+ \pi^-$

T. Aaltonen,[21] B. Álvarez González,[9,aa] S. Amerio,[40a] D. Amidei,[32] A. Anastassov,[15,y] A. Annovi,[17] J. Antos,[12]
G. Apollinari,[15] J. A. Appel,[15] T. Arisawa,[54] A. Artikov,[13] J. Asaadi,[49] W. Ashmanskas,[15] B. Auerbach,[57] A. Aurisano,[49]
F. Azfar,[39] W. Badgett,[15] T. Bae,[25] A. Barbaro-Galtieri,[26] V. E. Barnes,[44] B. A. Barnett,[23] P. Barria,[42c,42a] P. Bartos,[12]
M. Bauce,[40b,40a] F. Bedeschi,[42a] S. Behari,[23] G. Bellettini,[42b,42a] J. Bellinger,[56] D. Benjamin,[14] A. Beretvas,[15] A. Bhatti,[46]
D. Bisello,[40b,40a] I. Bizjak,[28] K. R. Bland,[5] B. Blumenfeld,[23] A. Bocci,[14] A. Bodek,[45] D. Bortoletto,[44] J. Boudreau,[43]
A. Boveia,[11] L. Brigliadori,[6b,6a] C. Bromberg,[33] E. Brucken,[21] J. Budagov,[13] H. S. Budd,[45] K. Burkett,[15] G. Busetto,[40b,40a]
P. Bussey,[19] A. Buzatu,[31] A. Calamba,[10] C. Calancha,[29] S. Camarda,[4] M. Campanelli,[28] M. Campbell,[32] F. Canelli,[11,15]
B. Carls,[22] D. Carlsmith,[56] R. Carosi,[42a] S. Carrillo,[16,n] S. Carron,[15] B. Casal,[9,l] M. Casarsa,[50a] A. Castro,[6b,6a] P. Catastini,[20]
D. Cauz,[50a] V. Cavaliere,[22] M. Cavalli-Sforza,[4] A. Cerri,[26,g] L. Cerrito,[28,t] Y. C. Chen,[1] M. Chertok,[7] G. Chiarelli,[42a]
G. Chlachidze,[15] F. Chlebana,[15] K. Cho,[25] D. Chokheli,[13] W. H. Chung,[56] Y. S. Chung,[45] M. A. Ciocci,[42c,42a] A. Clark,[18]
C. Clarke,[55] G. Compostella,[40b,40a] M. E. Convery,[15] J. Conway,[7] M. Corbo,[15] M. Cordelli,[17] C. A. Cox,[7] D. J. Cox,[7]
F. Crescioli,[42b,42a] J. Cuevas,[9,aa] R. Culbertson,[15] D. Dagenhart,[15] N. d'Ascenzo,[15,x] M. Datta,[15] P. de Barbaro,[45]
M. Dell'Orso,[42b,42a] L. Demortier,[46] M. Deninno,[6a] F. Devoto,[21] M. d'Errico,[40b,40a] A. Di Canto,[42b,42a] B. Di Ruzza,[15]
J. R. Dittmann,[5] M. D'Onofrio,[27] S. Donati,[42b,42a] P. Dong,[15] M. Dorigo,[50a] T. Dorigo,[40a] K. Ebina,[54] A. Elagin,[49] A. Eppig,[32]
R. Erbacher,[7] S. Errede,[22] N. Ershaidat,[15,ee] R. Eusebi,[49] S. Farrington,[39] M. Feindt,[24] J. P. Fernandez,[29] R. Field,[16]
G. Flanagan,[15,v] R. Forrest,[7] M. J. Frank,[5] M. Franklin,[20] J. C. Freeman,[15] Y. Funakoshi,[54] I. Furic,[16] M. Gallinaro,[46]
J. E. Garcia,[18] A. F. Garfinkel,[44] P. Garosi,[42c,42a] H. Gerberich,[22] E. Gerchtein,[15] S. Giagu,[47a] V. Giakoumopoulou,[3]
P. Giannetti,[42a] K. Gibson,[43] C. M. Ginsburg,[15] N. Giokaris,[3] P. Giromini,[17] G. Giurgiu,[23] V. Glagolev,[13] D. Glenzinski,[15]
M. Gold,[35] D. Goldin,[49] N. Goldschmidt,[16] A. Golossanov,[15] G. Gomez,[9] G. Gomez-Ceballos,[30] M. Goncharov,[30]
O. González,[29] I. Gorelov,[35] A. T. Goshaw,[14] K. Goulianos,[46] S. Grinstein,[4] C. Grosso-Pilcher,[11] R. C. Group,[53,15]
J. Guimaraes da Costa,[20] S. R. Hahn,[15] E. Halkiadakis,[48] A. Hamaguchi,[38] J. Y. Han,[45] F. Happacher,[17] K. Hara,[51] D. Hare,[48]
M. Hare,[52] R. F. Harr,[55] K. Hatakeyama,[5] C. Hays,[39] M. Heck,[24] J. Heinrich,[41] M. Herndon,[56] S. Hewamanage,[5] A. Hocker,[15]
W. Hopkins,[15,h] D. Horn,[24] S. Hou,[1] R. E. Hughes,[36] M. Hurwitz,[11] U. Husemann,[57] N. Hussain,[31] M. Hussein,[33] J. Huston,[33]
G. Introzzi,[42a] M. Iori,[47b,47a] A. Ivanov,[7,q] E. James,[15] D. Jang,[10] B. Jayatilaka,[14] E. J. Jeon,[25] S. Jindariani,[15] M. Jones,[44]
K. K. Joo,[25] S. Y. Jun,[10] T. R. Junk,[15] T. Kamon,[25,49] P. E. Karchin,[55] A. Kasmi,[5] Y. Kato,[38,p] W. Ketchum,[11] J. Keung,[41]
V. Khotilovich,[49] B. Kilminster,[15] D. H. Kim,[25] H. S. Kim,[25] J. E. Kim,[25] M. J. Kim,[17] S. B. Kim,[25] S. H. Kim,[51] Y. K. Kim,[11]
Y. J. Kim,[25] N. Kimura,[54] M. Kirby,[15] S. Klimenko,[16] K. Knoepfel,[15] K. Kondo,[54,a] D. J. Kong,[25] J. Konigsberg,[16]
A. V. Kotwal,[14] M. Kreps,[24,ff] J. Kroll,[41] D. Krop,[11] M. Kruse,[14] V. Krutelyov,[49,d] T. Kuhr,[24] M. Kurata,[51] S. Kwang,[11]
A. T. Laasanen,[44] S. Lami,[42a] S. Lammel,[15] M. Lancaster,[28] R. L. Lander,[7] K. Lannon,[36,z] A. Lath,[48] G. Latino,[42c,42a]
T. LeCompte,[2] E. Lee,[49] H. S. Lee,[11,r] J. S. Lee,[25] S. W. Lee,[49,cc] S. Leo,[42b,42a] S. Leone,[42a] J. D. Lewis,[15] A. Limosani,[14,u]
C.-J. Lin,[26] M. Lindgren,[15] E. Lipeles,[41] A. Lister,[18] D. O. Litvintsev,[15] C. Liu,[43] H. Liu,[53] Q. Liu,[44] T. Liu,[15] S. Lockwitz,[57]
A. Loginov,[57] D. Lucchesi,[40b,40a] J. Lueck,[24] P. Lujan,[26] P. Lukens,[15] G. Lungu,[46] J. Lys,[26] R. Lysak,[12,f] R. Madrak,[15]
K. Maeshima,[15] P. Maestro,[42c,42a] S. Malik,[46] G. Manca,[27,b] A. Manousakis-Katsikakis,[3] F. Margaroli,[47a] C. Marino,[24]
M. Martínez,[4] P. Mastrandrea,[47a] K. Matera,[22] M. E. Mattson,[55] A. Mazzacane,[15] P. Mazzanti,[6a] K. S. McFarland,[45]
P. McIntyre,[49] R. McNulty,[27,k] A. Mehta,[27] P. Mehtala,[21] C. Mesropian,[46] T. Miao,[15] D. Mietlicki,[32] A. Mitra,[1] H. Miyake,[51]
S. Moed,[15] N. Moggi,[6a] M. N. Mondragon,[15,n] C. S. Moon,[25] R. Moore,[15] M. J. Morello,[42d,42a] J. Morlock,[24]
P. Movilla Fernandez,[15] A. Mukherjee,[15] Th. Muller,[24] P. Murat,[15] M. Mussini,[6b,6a] J. Nachtman,[15,o] Y. Nagai,[51]
J. Naganoma,[54] I. Nakano,[37] A. Napier,[52] J. Nett,[49] C. Neu,[53] M. S. Neubauer,[22] J. Nielsen,[26,e] L. Nodulman,[2] S. Y. Noh,[25]
O. Norniella,[22] L. Oakes,[39] S. H. Oh,[14] Y. D. Oh,[25] I. Oksuzian,[53] T. Okusawa,[38] R. Orava,[21] L. Ortolan,[4] S. Pagan Griso,[40b,40a]
C. Pagliarone,[50a] E. Palencia,[9,g] V. Papadimitriou,[15] A. A. Paramonov,[2] J. Patrick,[15] G. Pauletta,[50b,50a] M. Paulini,[10] C. Paus,[30]
D. E. Pellett,[7] A. Penzo,[50a] T. J. Phillips,[14] G. Piacentino,[42a] E. Pianori,[41] J. Pilot,[36] K. Pitts,[22] C. Plager,[8] L. Pondrom,[56]
S. Poprocki,[15,h] K. Potamianos,[44] F. Prokoshin,[13,dd] A. Pranko,[26] F. Ptohos,[17,i] G. Punzi,[42b,42a] A. Rahaman,[43]
V. Ramakrishnan,[56] N. Ranjan,[44] I. Redondo,[29] P. Renton,[39] M. Rescigno,[47a] T. Riddick,[28] F. Rimondi,[6b,6a] L. Ristori,[42a,15]
A. Robson,[19] T. Rodrigo,[9] T. Rodriguez,[41] E. Rogers,[22] S. Rolli,[52,j] R. Roser,[15] F. Ruffini,[42c,42a] A. Ruiz,[9] J. Russ,[10] V. Rusu,[15]
A. Safonov,[49] W. K. Sakumoto,[45] Y. Sakurai,[54] L. Santi,[50b,50a] K. Sato,[51] V. Saveliev,[15,x] A. Savoy-Navarro,[15,bb]
P. Schlabach,[15] A. Schmidt,[24] E. E. Schmidt,[15] T. Schwarz,[15] L. Scodellaro,[9] A. Scribano,[42c,42a] F. Scuri,[42a] S. Seidel,[35]
Y. Seiya,[38] A. Semenov,[13] F. Sforza,[42b,42a] S. Z. Shalhout,[7] T. Shears,[27] P. F. Shepard,[43] M. Shimojima,[51,w] M. Shochet,[11]
I. Shreyber-Tecker,[34] A. Simonenko,[13] P. Sinervo,[31] K. Sliwa,[52] J. R. Smith,[7] F. D. Snider,[15] A. Soha,[15] V. Sorin,[4] H. Song,[43]
P. Squillacioti,[42c,42a] M. Stancari,[15] R. St. Denis,[19] B. Stelzer,[31] O. Stelzer-Chilton,[31] D. Stentz,[15,y] J. Strologas,[35]

G. L. Strycker,[32] Y. Sudo,[51] A. Sukhanov,[15] I. Suslov,[13] K. Takemasa,[51] Y. Takeuchi,[51] J. Tang,[11] M. Tecchio,[32] P. K. Teng,[1] J. Thom,[15,h] J. Thome,[10] G. A. Thompson,[22] E. Thomson,[41] D. Toback,[49] S. Tokar,[12] K. Tollefson,[33] T. Tomura,[51] D. Tonelli,[15] S. Torre,[17] D. Torretta,[15] P. Totaro,[40a] M. Trovato,[42d,42a] F. Ukegawa,[51] S. Uozumi,[25] A. Varganov,[32] F. Vázquez,[16,n] G. Velev,[15] C. Vellidis,[15] M. Vidal,[44] I. Vila,[9] R. Vilar,[9] J. Vizán,[9] M. Vogel,[35] G. Volpi,[17] P. Wagner,[41] R. L. Wagner,[15] T. Wakisaka,[38] R. Wallny,[8] S. M. Wang,[1] A. Warburton,[31] D. Waters,[28] W. C. Wester III,[15] D. Whiteson,[41,c] A. B. Wicklund,[2] E. Wicklund,[15] S. Wilbur,[11] F. Wick,[24] H. H. Williams,[41] J. S. Wilson,[36] P. Wilson,[15] B. L. Winer,[36] P. Wittich,[15,h] S. Wolbers,[15] H. Wolfe,[36] T. Wright,[32] X. Wu,[18] Z. Wu,[5] K. Yamamoto,[38] D. Yamato,[38] T. Yang,[15] U. K. Yang,[11,s] Y. C. Yang,[25] W.-M. Yao,[26] G. P. Yeh,[15] K. Yi,[15,o] J. Yoh,[15] K. Yorita,[54] T. Yoshida,[38,m] G. B. Yu,[14] I. Yu,[25] S. S. Yu,[15] J. C. Yun,[15] A. Zanetti,[50a] Y. Zeng,[14] C. Zhou,[14] and S. Zucchelli[6b,6a]

(CDF Collaboration)

[1]*Institute of Physics, Academia Sinica, Taipei, Taiwan 11529, Republic of China*
[2]*Argonne National Laboratory, Argonne, Illinois 60439, USA*
[3]*University of Athens, 157 71 Athens, Greece*
[4]*Institut de Fisica d'Altes Energies, ICREA, Universitat Autonoma de Barcelona, E-08193, Bellaterra (Barcelona), Spain*
[5]*Baylor University, Waco, Texas 76798, USA*
[6a]*Istituto Nazionale di Fisica Nucleare Bologna, I-40127 Bologna, Italy*
[6b]*University of Bologna, I-40127 Bologna, Italy*
[7]*University of California, Davis, Davis, California 95616, USA*
[8]*University of California, Los Angeles, Los Angeles, California 90024, USA*
[9]*Instituto de Fisica de Cantabria, CSIC-University of Cantabria, 39005 Santander, Spain*
[10]*Carnegie Mellon University, Pittsburgh, Pennsylvania 15213, USA*
[11]*Enrico Fermi Institute, University of Chicago, Chicago, Illinois 60637, USA*
[12]*Comenius University, 842 48 Bratislava, Slovakia; Institute of Experimental Physics, 040 01 Kosice, Slovakia*
[13]*Joint Institute for Nuclear Research, RU-141980 Dubna, Russia*
[14]*Duke University, Durham, North Carolina 27708, USA*
[15]*Fermi National Accelerator Laboratory, Batavia, Illinois 60510, USA*
[16]*University of Florida, Gainesville, Florida 32611, USA*
[17]*Laboratori Nazionali di Frascati, Istituto Nazionale di Fisica Nucleare, I-00044 Frascati, Italy*
[18]*University of Geneva, CH-1211 Geneva 4, Switzerland*
[19]*Glasgow University, Glasgow G12 8QQ, United Kingdom*
[20]*Harvard University, Cambridge, Massachusetts 02138, USA*
[21]*Division of High Energy Physics, Department of Physics, University of Helsinki*
and Helsinki Institute of Physics, FIN-00014, Helsinki, Finland
[22]*University of Illinois, Urbana, Illinois 61801, USA*
[23]*The Johns Hopkins University, Baltimore, Maryland 21218, USA*
[24]*Institut für Experimentelle Kernphysik, Karlsruhe Institute of Technology, D-76131 Karlsruhe, Germany*
[25]*Center for High Energy Physics: Kyungpook National University, Daegu 702-701, Korea;*
Seoul National University, Seoul 151-742, Korea; Sungkyunkwan University, Suwon 440-746, Korea;
Korea Institute of Science and Technology Information, Daejeon 305-806, Korea;
Chonnam National University, Gwangju 500-757, Korea; Chonbuk National University, Jeonju 561-756, Korea
[26]*Ernest Orlando Lawrence Berkeley National Laboratory, Berkeley, California 94720, USA*
[27]*University of Liverpool, Liverpool L69 7ZE, United Kingdom*
[28]*University College London, London WC1E 6BT, United Kingdom*
[29]*Centro de Investigaciones Energeticas Medioambientales y Tecnologicas, E-28040 Madrid, Spain*
[30]*Massachusetts Institute of Technology, Cambridge, Massachusetts 02139, USA*
[31]*Institute of Particle Physics: McGill University, Montréal, Québec, Canada H3A 2T8;*
Simon Fraser University, Burnaby, British Columbia, Canada V5A 1S6; University of Toronto, Toronto, Ontario, Canada M5S 1A7;
and TRIUMF, Vancouver, British Columbia, Canada V6T 2A3
[32]*University of Michigan, Ann Arbor, Michigan 48109, USA*
[33]*Michigan State University, East Lansing, Michigan 48824, USA*
[34]*Institution for Theoretical and Experimental Physics, ITEP, Moscow 117259, Russia*
[35]*University of New Mexico, Albuquerque, New Mexico 87131, USA*
[36]*The Ohio State University, Columbus, Ohio 43210, USA*
[37]*Okayama University, Okayama 700-8530, Japan*
[38]*Osaka City University, Osaka 588, Japan*
[39]*University of Oxford, Oxford OX1 3RH, United Kingdom*

[40a]*Istituto Nazionale di Fisica Nucleare, Sezione di Padova-Trento, I-35131 Padova, Italy*
[40b]*University of Padova, I-35131 Padova, Italy*
[41]*University of Pennsylvania, Philadelphia, Pennsylvania 19104, USA*
[42a]*Istituto Nazionale di Fisica Nucleare Pisa, I-56127 Pisa, Italy*
[42b]*University of Pisa, I-56127 Pisa, Italy*
[42c]*University of Siena, I-56127 Pisa, Italy*
[42d]*Scuola Normale Superiore, I-56127 Pisa, Italy*
[43]*University of Pittsburgh, Pittsburgh, Pennsylvania 15260, USA*
[44]*Purdue University, West Lafayette, Indiana 47907, USA*
[45]*University of Rochester, Rochester, New York 14627, USA*
[46]*The Rockefeller University, New York, New York 10065, USA*
[47a]*Istituto Nazionale di Fisica Nucleare, Sezione di Roma 1, I-00185 Roma, Italy*
[47b]*Sapienza Università di Roma, I-00185 Roma, Italy*
[48]*Rutgers University, Piscataway, New Jersey 08855, USA*
[49]*Texas A&M University, College Station, Texas 77843, USA*
[50a]*Istituto Nazionale di Fisica Nucleare Trieste/Udine, I-34100 Trieste, Italy*
[50b]*University of Udine, I-33100 Udine, Italy*
[51]*University of Tsukuba, Tsukuba, Ibaraki 305, Japan*
[52]*Tufts University, Medford, Massachusetts 02155, USA*
[53]*University of Virginia, Charlottesville, Virginia 22906, USA*
[54]*Waseda University, Tokyo 169, Japan*
[55]*Wayne State University, Detroit, Michigan 48201, USA*
[56]*University of Wisconsin, Madison, Wisconsin 53706, USA*
[57]*Yale University, New Haven, Connecticut 06520, USA*
(Received 5 July 2012; published 13 August 2012)

We report a measurement of time-integrated *CP*-violation asymmetries in the resonant substructure of the three-body decay $D^0 \to K_S^0 \pi^+ \pi^-$ using CDF II data corresponding to 6.0 fb^{-1} of integrated luminosity from Tevatron $p\bar{p}$ collisions at $\sqrt{s} = 1.96$ TeV. The charm mesons used in this analysis come from $D^{*+}(2010) \to D^0\pi^+$ and $D^{*-}(2010) \to \bar{D}^0\pi^-$, where the production flavor of the charm

———————

[a]Deceased.
[b]Visitor from Istituto Nazionale di Fisica Nucleare, Sezione di Cagliari, 09042 Monserrato (Cagliari), Italy.
[c]Visitor from University of California Irvine, Irvine, CA 92697, USA.
[d]Visitor from University of California Santa Barbara, Santa Barbara, CA 93106, USA.
[e]Visitor from University of California Santa Cruz, Santa Cruz, CA 95064, USA.
[f]Visitor from Institute of Physics, Academy of Sciences of the Czech Republic, Czech Republic.
[g]Visitor from CERN, CH-1211 Geneva, Switzerland.
[h]Visitor from Cornell University, Ithaca, NY 14853, USA.
[i]Visitor from University of Cyprus, Nicosia CY-1678, Cyprus.
[j]Visitor from Office of Science, U.S. Department of Energy, Washington, DC 20585, USA.
[k]Visitor from University College Dublin, Dublin 4, Ireland.
[l]Visitor from ETH, 8092 Zurich, Switzerland.
[m]Visitor from University of Fukui, Fukui City, Fukui Prefecture, Japan 910-0017.
[n]Visitor from Universidad Iberoamericana, Mexico D.F., Mexico.
[o]Visitor from University of Iowa, Iowa City, IA 52242, USA.
[p]Visitor from Kinki University, Higashi-Osaka City, Japan 577-8502.
[q]Visitor from Kansas State University, Manhattan, KS 66506, USA.
[r]Visitor from Ewha Womans University, Seoul, 120-750, Korea.
[s]Visitor from University of Manchester, Manchester M13 9PL, United Kingdom.
[t]Visitor from Queen Mary, University of London, London, E1 4NS, United Kingdom.
[u]Visitor from University of Melbourne, Victoria 3010, Australia.
[v]Visitor from Muons, Inc., Batavia, IL 60510, USA.
[w]Visitor from Nagasaki Institute of Applied Science, Nagasaki, Japan.
[x]Visitor from National Research Nuclear University, Moscow, Russia.
[y]Visitor from Northwestern University, Evanston, IL 60208, USA.
[z]Visitor from University of Notre Dame, Notre Dame, IN 46556, USA.
[aa]Visitor from Universidad de Oviedo, E-33007 Oviedo, Spain.
[bb]Visitor from CNRS-IN2P3, Paris, F-75205 France.
[cc]Visitor from Texas Tech University, Lubbock, TX 79609, USA.
[dd]Visitor from Universidad Tecnica Federico Santa Maria, 110v Valparaiso, Chile.
[ee]Visitor from Yarmouk University, Irbid 211-63, Jordan.
[ff]Visitor from University of Warwick, Coventry CV4 7AL, United Kingdom.

meson is determined by the charge of the accompanying pion. We apply a Dalitz-amplitude analysis for the description of the dynamic decay structure and use two complementary approaches, namely, a full Dalitz-plot fit employing the isobar model for the contributing resonances and a model-independent bin-by-bin comparison of the D^0 and $\bar{D}^0$ Dalitz plots. We find no *CP*-violation effects and measure an asymmetry of $A_{CP} = (-0.05 \pm 0.57(\text{stat}) \pm 0.54(\text{syst}))\%$ for the overall integrated *CP*-violation asymmetry, consistent with the standard model prediction.

I. INTRODUCTION

The phenomenon of *CP* violation is well established for weakly decaying hadrons consisting of down-type quarks. It has been observed with mixing (indirect *CP* violation) and without mixing (direct *CP* violation) in decays of the K^0 and B^0 mesons, and confirms the theory of Kobayashi and Maskawa [1] that describes *CP* violation in the standard model. For charm mesons, *CP*-violation effects are expected to be small. The lack of experimental observation of *CP* violation in charm meson decays is consistent with the expectation. Only recently the LHCb Collaboration has reported the first evidence for *CP* violation in the time-integrated rate of D^0 decays to two hadrons at $\mathcal{O}(10^{-2})$ [2], which was consequently confirmed by the CDF Collaboration [3]. Whether this is consistent with the standard model expectation or a hint for new physics is not yet clear. Therefore, it is important to complement the LHCb result with measurements of *CP* asymmetries in other D^0 decay modes.

In this article, we describe a search for *CP* violation in time-integrated decay rates of D^0 mesons to the $K^0_S \pi^+ \pi^-$ final state. The standard model expectations for the size of time-integrated *CP*-violation asymmetries in $K^0_S \pi^+ \pi^-$ decays are $\mathcal{O}(10^{-6})$, where the dominant contribution arises from *CP* violation in K^0-$\bar{K}^0$ mixing [4,5]. The observation of any significantly larger asymmetries would be a strong hint for physics beyond the standard model.

The CLEO Collaboration performed a dedicated search for time-integrated *CP* violation in a fit to the Dalitz plot of the $D^0/\bar{D}^0$ three-body decay to $K^0_S \pi^+ \pi^-$ [6]. Belle and *BABAR* allowed for *CP* violation in their measurements of the D^0-$\bar{D}^0$ mixing parameters [7,8]. Up to now, no *CP*-violation effects have been found [9].

In this analysis, we exploit a large sample of $D^*(2010)^\pm$ decays, reconstructed in a data set corresponding to 6.0 fb^{-1} of integrated luminosity produced in $p\bar{p}$ collisions at $\sqrt{s} = 1.96$ TeV and collected by the CDF II detector, to measure time-integrated *CP*-violation asymmetries in the resonant substructure of the decay $D^0/\bar{D}^0 \to K^0_S \pi^+ \pi^-$. The neutral D meson production flavor is determined by the charge of the pion in the $D^{*+}(2010) \to D^0 \pi^+$ and $D^{*-}(2010) \to \bar{D}^0 \pi^-$ decays (D^* tagging). Throughout the rest of the paper the use of a specific particle state implies the use of the charge-conjugate state as well, unless explicitly noted. For brevity, $D^*(2010)^+$ is abbreviated as D^{*+}.

In Secs. II and III we briefly describe the CDF II detector and the trigger components important for this analysis. In Secs. IV and V we describe the off-line candidate reconstruction and selection, respectively. In Sec. VI we explain the Dalitz-plot fits of the resonant substructure of the decay, followed by a discussion of systematic uncertainties in Sec. VII and a presentation of the results in Sec. VIII. In Sec. IX we describe a model-independent search for *CP* asymmetries using a bin-by-bin comparison of Dalitz plots [10], followed by the conclusion in Sec. X.

II. CDF II DETECTOR

The analysis is performed on a data set collected with the CDF II detector [11] between February 2002 and February 2010, corresponding to an integrated luminosity of 6.0 fb^{-1} of $p\bar{p}$ collisions. Among the components and capabilities of the detector, the charged particle tracking is the one most relevant to this analysis. The tracking system lies within a uniform, axial magnetic field of 1.4 T. The inner tracking volume, up to a radius of 28 cm, is composed of six or seven layers, depending on polar angle, of double-sided silicon microstrip detectors [12,13]. An additional single-sided silicon layer is mounted directly on the beam pipe at a radius of 1.5 cm [14], allowing excellent resolution of the transverse impact parameter d_0, defined as the distance of closest approach of a charged particle trajectory (track) to the interaction point in the plane transverse to the beam line. The silicon detector allows the identification of displaced, secondary vertices from bottom-hadron and charm-hadron decays with a resolution of approximately 30 μm in the transverse and 70 μm in the longitudinal direction. The outer tracking volume from a radius of 40 to 137 cm is occupied by an open-cell argon-ethane gas drift chamber (COT) [15]. An important aspect for this analysis is that the layout of the COT is intrinsically charge-asymmetric because of an about 35° tilt angle between the cell orientation and the radial direction. The total tracking system provides a transverse momentum resolution of $\sigma(p_T)/p_T^2 \approx 0.07\%$ (GeV/c)$^{-1}$ for tracks with $p_T > 2$ GeV/c. A more detailed description of the tracking system can be found in Ref. [16].

III. ON-LINE EVENT SELECTION

A three-level event-selection system (trigger) is used. At level 1, a hardware track processor [17] identifies charged

particles using information from the COT and measures their transverse momenta and azimuthal angles around the beam direction. The basic requirement at level 1 is the presence of two charged particles, each with $p_T > 2$ GeV/c. At level 2, the silicon vertex trigger [18] adds silicon-hit information to the tracks found by the hardware track processor, thus allowing the precise measurement of impact parameters of tracks. The two level-1 tracks are required to have impact parameters between 0.1 and 1 mm, an opening angle in the transverse plane between 2° and 90°, and to be consistent with coming from a common vertex displaced from the interaction point by at least 200 μm in the plane transverse to the beam line. This is complemented by a selection without the vertex displacement requirement, collecting events with low invariant-mass track pairs having opening angles less than 6°. The level-3 trigger is implemented in software and provides the final on-line selection by confirming the first two trigger-level decisions using a more precise reconstruction. This trigger is designed to collect hadronic decays of long-lived particles such as b and c hadrons. Three different configurations of this trigger are employed, requiring a minimum on the scalar sum of the transverse momenta of the two trigger tracks of 4.0, 5.5, and 6.5 GeV/c. The active threshold depends on the instantaneous luminosity conditions, with higher thresholds used at higher instantaneous luminosity to reduce the higher trigger accept rate.

IV. OFF-LINE EVENT RECONSTRUCTION

The off-line reconstruction of candidates starts by fitting tracks taking into account multiple scattering and ionization energy loss calculated for the pion mass hypothesis. Since all final state particles in the studied decay chain are pions, we assign the pion mass to each track in the following steps. Two oppositely charged tracks are combined to form a K_S^0 candidate. To construct D^0 candidates, each K_S^0 candidate is combined with all other possible oppositely charged track pairs found in the event. Finally, the D^{*+} candidates are obtained by combining each D^0 candidate with one of the remaining tracks in the event. The tracks forming the K_S^0, D^0, and D^{*+} candidates are subjected to separate kinematic fits that constrain them to originate from a common decay point in each case, resulting in three reconstructed decay points for the considered decay chain. In each step of the reconstruction, standard quality requirements on tracks and vertices are used to ensure well-measured momenta and decay positions [19].

V. CANDIDATE SELECTION

For the selection of the candidates, we first impose some quality requirements to suppress the most obvious backgrounds, such as random combinations of low-p_T particles, D^{*+} pions strongly displaced from the interaction point, or short-lived D^0 candidates without proper secondary-vertex

separation. We require the transverse momentum of each pion to be greater than 400 MeV/c, the transverse momentum of the D^{*+} to exceed 5.0 GeV/c, the impact parameter of the pion from the D^{*+} decay divided by its uncertainty $d_0/\sigma_{d_0}(\pi_{D^{*+}})$ not to exceed 15, and the transverse decay length of the D^0 candidate projected into the transverse momentum (L_{xy}) to exceed its resolution ($\sigma_{L_{xy}}$). For the surviving candidates we use an artificial neural network to distinguish signal from background. The neural network is constructed with the NeuroBayes package [20] and trained, using data only, by means of the $_s\mathcal{P}$lot technique [21]. This technique assigns a weight to each candidate, proportional to the probability that the candidate is signal. The candidate weight is based on a discriminating variable, which is required to be independent of the ones used in the neural network training. In our case, the discriminating variable is the mass difference $\Delta M = M(K_S^0\pi^+\pi^-\pi^+) - M(K_S^0\pi^+\pi^-)$ of the D^{*+} candidate. In the training, each candidate enters with a weight calculated from the signal probability that is derived from its mass. Based on these weights, the neural network learns the features of signal and background events. Since we use only data for the neural network training, we randomly split each sample into two parts evenly distributed in data taking time and train two networks. Each network is then applied to the complementary subsample in order for the selection to be trained on a sample independent from the one to which it is applied. This approach avoids a bias of the selection originating from statistical fluctuations possibly learned by the network. The method of NeuroBayes $_s\mathcal{P}$lot trainings was first applied in our previous work on charm baryons [22].

The network uses five input variables. Ordered by decreasing importance, these are $L_{xy}/\sigma_{L_{xy}}(D^0)$, the χ^2 quality of the D^{*+} vertex fit, $d_0/\sigma_{d_0}(\pi_{D^{*+}})$, $p_T(\pi_{D^{*+}})$, and the reconstructed mass of the K_S^0 candidate. The D^{*+} network training is based on the mass difference distribution in the range $140 < \Delta M < 156$ MeV/c^2. A fit of a nonrelativistic Breit-Wigner convoluted with a Gaussian for the signal and a third-order polynomial for the background function defines the probability density functions used to calculate the $_s\mathcal{P}$lot weights. The final neural network output requirement is chosen to maximize $S/\sqrt{S+B}$, where S (B) is the estimated number of signal (background) events in the signal region estimated from a fit to the $M(K_S^0\pi^+\pi^-)$ distribution. The selected requirement corresponds to an *a posteriori* signal probability greater than 25%. In 11% of the selected events, multiple D^{*+} candidates are reconstructed for a single D^0 candidate. We choose the D^{*+} candidate that gives the most D^*-like neural network output and remove all others to avoid identical candidates populating the Dalitz space.

The $M(K_S^0\pi^+\pi^-)$ and ΔM distributions of the selected candidates are shown in Fig. 1, together with the corresponding fits to determine the signal and background yields. In the $K_S^0\pi^+\pi^-$ mass distribution, the D^0 signal

FIG. 2 (color online). Dalitz plot of the decay $D^0/\bar{D}^0 \rightarrow K_S^0 \pi^+ \pi^-$, where the squared invariant masses of the two-body combinations $K_S^0 \pi^\pm$(RS) and $\pi^+ \pi^-$ are chosen as kinematic quantities. The solid line indicates the kinematic boundaries.

The resonant substructure of a three-body decay can be described by means of a Dalitz-amplitude analysis [23]. The Dalitz plot of the considered decay $D^0 \rightarrow K_S^0 \pi^+ \pi^-$, composed of all selected candidates, is shown in Fig. 2. It represents the decay dynamics as a function of the squared invariant masses of the two-body combinations $K_S^0 \pi^\pm$(RS) and $\pi^+ \pi^-$, where the notation $K_S^0 \pi^\pm$(RS) expresses that the Cabibbo-favored combination, or right-sign (RS) pion, is used for both D^0 ($K_S^0 \pi^-$) and $\bar{D}^0$ ($K_S^0 \pi^+$) decays. The squared invariant mass of the doubly Cabibbo-suppressed or wrong-sign (WS) two-body combination $K_S^0 \pi^\pm$(WS) is a linear function of $M^2_{K_S^0 \pi^\pm \text{(RS)}}$ and $M^2_{\pi^+ \pi^-}$. Three types of final states contribute in the decay: Cabibbo-favored, doubly Cabibbo-suppressed, and CP eigenstates. The dominant decay mode is the Cabibbo-favored $D^0 \rightarrow K^*(892)^- \pi^+$, which amounts for about 60% of the total branching fraction. The second largest contribution is from the intermediate CP eigenstate $K_S^0 \rho(770)$, which is color-suppressed compared to $K^*(892)^- \pi^+$.

VI. DALITZ ANALYSIS

A simultaneous fit to the resonant substructure of the decay to $K_S^0 \pi^+ \pi^-$ is performed on the combined D^0 and $\bar{D}^0$ samples to determine the sizes of the various contributions. These are compared with previous results from other experiments to build confidence in the fitting technique. Then the fit is applied independently to D^*-tagged D^0 and $\bar{D}^0$ samples to measure CP-violation asymmetries in the decay amplitudes for each subprocess.

A. Fit to the combined sample

A binned maximum-likelihood fit to the two-dimensional Dalitz-plot distribution with bin widths of 0.025 GeV$^2/c^4$ in both dimensions is performed to determine the contributions of the various intermediate resonances. The likelihood function has the general form
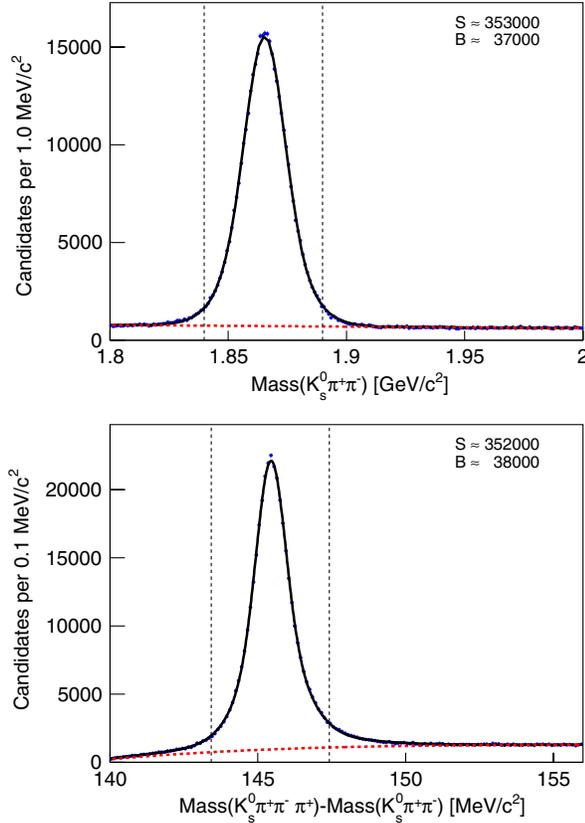
FIG. 1 (color online). The $M(K_S^0 \pi^+ \pi^-)$ and ΔM data distributions (points with error bars) with fit results overlaid. The dashed lines correspond to the background contributions. The vertical lines indicate signal ranges used for further analysis. The $M(K_S^0 \pi^+ \pi^-)$ (ΔM) distribution contains only candidates populating the signal ΔM [$M(K_S^0 \pi^+ \pi^-)$] range.

is described by the sum of two Gaussian functions with common mean, and the background is modeled by a linear function. The D^{*+} signal in the ΔM distribution is described by a nonrelativistic Breit-Wigner convoluted with a resolution function. The latter is determined from simulated events and consists of the weighted sum of three Gaussian functions to model the more complicated shape of the resolution close to the kinematic threshold in the ΔM distribution. The background is modeled by a third-order polynomial.

For the Dalitz-plot studies, the analysis is restricted to candidates populating two mass ranges, $1.84 < M(K_S^0 \pi^+ \pi^-) < 1.89$ GeV/c^2 and $143.4 < \Delta M < 147.4$ MeV/c^2, indicated by the dashed vertical lines in Fig. 1. The selected data sample contains approximately 3.5×10^5 signal events and consists of about 90% correctly D^*-tagged D^0 signal, 1% mistagged D^0 signal, and 9% background candidates. A mistag results from the combination of a D^0 with a random, wrongly charged pion not originating from a $D^{*\pm}$ decay. The mistag fraction is estimated by a dedicated parameter in the Dalitz-plot fit described in Sec. VI A.
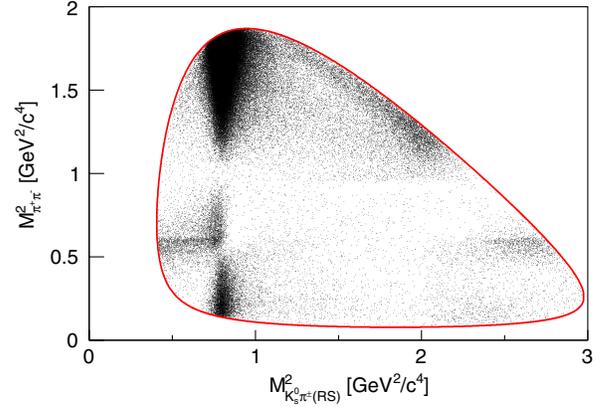
$$\mathcal{L}(\vec{\theta}) = \prod_{i=1}^{I} \frac{\mu_i^{n_i} e^{-\mu_i}}{n_i!}, \tag{1}$$

where $\vec{\theta}$ are the estimated parameters, I is the number of bins, n_i is the number of entries in bin i, and μ_i is the expected number of entries in bin i. The latter are obtained using the function

$$\mu(M^2_{K^0_S\pi^\pm(\text{RS})}, M^2_{\pi^+\pi^-}) = N[T\epsilon(M^2_{K^0_S\pi^\pm(\text{RS})}, M^2_{\pi^+\pi^-})|\mathcal{M}(M^2_{K^0_S\pi^\pm(\text{RS})}, M^2_{\pi^+\pi^-})|^2$$
$$+ (1-T)\epsilon(M^2_{K^0_S\pi^\pm(\text{RS})}, M^2_{\pi^+\pi^-})|\mathcal{M}(M^2_{K^0_S\pi^\pm(\text{WS})}, M^2_{\pi^+\pi^-})|^2] + B(M^2_{K^0_S\pi^\pm(\text{RS})}, M^2_{\pi^+\pi^-}), \tag{2}$$

where $\mathcal{M}$ is the complex matrix element of the decay, $(1-T)$ is the fraction of D^0 candidates with wrongly determined production flavor, called the mistag fraction, N is the normalization of the number of signal events, $\epsilon(M^2_{K^0_S\pi^\pm(\text{RS})}, M^2_{\pi^+\pi^-})$ is the relative trigger and reconstruction efficiency over the Dalitz plot, and $B(M^2_{K^0_S\pi^\pm(\text{RS})}, M^2_{\pi^+\pi^-})$ is the background distribution. The function is evaluated at the bin center to calculate the expectation for μ_i.

The isobar model [24] is used to describe the matrix element $\mathcal{M}$. The various resonances are modeled by complex numbers $a_j e^{i\delta_j}$, where j refers to the jth isobar composed of the amplitude a_j and the phase δ_j, multiplied with the individual complex matrix element $\mathcal{A}_j(M, \Gamma)$, which depends on the mass M and decay width Γ of the resonance. The phase convention is the same as in the CLEO analysis [6] and described in Ref. [19]. The complex numbers are added as

$$\mathcal{M} = a_0 e^{i\delta_0} + \sum_j a_j e^{i\delta_j} \mathcal{A}_j(M, \Gamma), \tag{3}$$

where $a_0 e^{i\delta_0}$ represents a possible nonresonant contribution. Since a_j and δ_j are relative amplitudes and phases, one resonance can be chosen as the reference. The amplitude and phase of the $\rho(770)$, being the largest color-suppressed mode, are fixed to the values $a_{\rho(770)} = 1$ and $\delta_{\rho(770)} = 0$, respectively. The individual matrix elements, $\mathcal{A}_j(M, \Gamma)$, correspond to normalized Breit-Wigner shapes with Blatt-Weisskopf form factors [25]. A more detailed description can be found in Ref. [26]. For the intermediate resonances $\rho(770)$ and $\rho(1450)$ decaying to $\pi^+\pi^-$, the Breit-Wigner shape is replaced by the Gounaris-Sakurai description [27].

To account for the limited accuracy of the knowledge on the masses and widths of the intermediate resonances, these parameters can vary within their experimental uncertainties, taken from Ref. [28] for the $f_0(980)$ and $f_0(1370)$ mesons, and Ref. [29] for the others. This is accomplished by means of Gaussian constraints in the likelihood function, except for the resonances $K^*(892)^\pm$, $f_0(600)$, and σ_2, which are unconstrained. Because the $K^*(892)^\pm$ is the most prominent resonance, with its 60% branching fraction, floating the $K^*(892)^\pm$ mass and width in the Dalitz-plot fit improves the fit quality. The reason for

the unconstrained $f_0(600)$ and σ_2 resonance parameters is the poorly known nature of these states. The scalar resonance σ_2 is introduced to account for a structure near $1 \text{ GeV}^2/c^4$ in the $M^2_{\pi^+\pi^-}$ distribution. A possible explanation for this structure, proposed in Ref. [30], is the decay $f_0(980) \rightarrow \eta\eta$ with rescattering of $\eta\eta$ to $\pi^+\pi^-$, resulting in a distortion of the $f_0(980) \rightarrow \pi^+\pi^-$ amplitude for $M^2_{\pi^+\pi^-}$ near the $\eta\eta$ production threshold. The masses and widths of the resonances $K^*(892)^\pm$, $K^*_0(1430)^\pm$, and $K^*_2(1430)^\pm$ are required to be identical for Cabibbo-favored and doubly Cabibbo-suppressed (DCS) processes.

Simulated events are used to estimate the relative reconstruction efficiency over the $D^0 \rightarrow K^0_S\pi^+\pi^-$ Dalitz plot. The considered decay chain, starting with D^{*+}, is simulated by means of the EVTGEN package [31], where the three-body decay structure of the D^0 is generated without any intermediate resonances. The generated events are passed through the detector simulation and reconstructed as data. The simulated detector and trigger acceptance influence the Dalitz-plot distribution in a complicated way. To estimate the efficiency, a binned maximum-likelihood fit to the Dalitz-plot distribution of simulated decays is performed, where a binning of $0.05 \text{ GeV}^2/c^4$ in both dimensions is used. An empiric function consisting of the sum of a ninth-order multinomial in $(M^2_{K^0_S\pi^\pm(\text{RS})})^m \times (M^2_{\pi^+\pi^-})^n$, where $m + n \leq 9$, and a Gaussian function,

$$\epsilon = E_0 + E_x M^2_{K^0_S\pi^\pm(\text{RS})} + E_y M^2_{\pi^+\pi^-} + E_{x^2}(M^2_{K^0_S\pi^\pm(\text{RS})})^2$$
$$+ E_{xy} M^2_{K^0_S\pi^\pm(\text{RS})} M^2_{\pi^+\pi^-} + E_{y^2}(M^2_{\pi^+\pi^-})^2$$
$$+ \cdots + G(M^2_{\pi^+\pi^-}), \tag{4}$$

is employed. The subscripts x and y are abbreviations for $M^2_{K^0_S\pi^\pm(\text{RS})}$ and $M^2_{\pi^+\pi^-}$, respectively. The Gaussian function $G(M^2_{\pi^+\pi^-})$ models the efficiency enhancement at low $M^2_{\pi^+\pi^-}$ values, which is caused by a trigger configuration that selects track pairs with small opening angle. The fit projections together with the corresponding mass-squared distributions of the three two-body combinations are shown in Fig. 3.

The background in the Dalitz-plot distribution receives three dominant contributions: combinatorial background of purely random particle combinations, misreconstructed
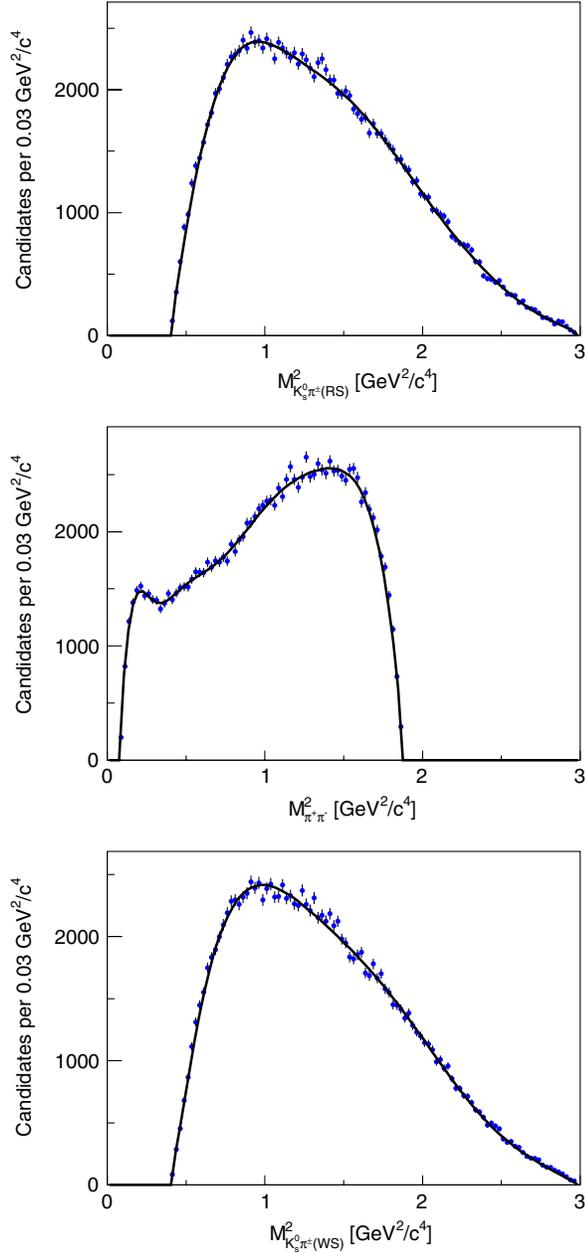
FIG. 3 (color online). Squared invariant-mass distributions of the simulated events used for the determination of the relative reconstruction efficiency over the Dalitz plot, together with the corresponding fit projections.

D^0 candidates peaking below the D^{*+} signal, and combinations of true D^0 candidates with a random pion. The first two are estimated in a sample chosen from the D^0-mass upper sideband $1.92 < M(K_S^0 \pi^+ \pi^-) < 1.95$ GeV/c^2 with the same selection requirements used in the signal region. The combinations of true D^0 candidates with a random pion are directly determined as the mistag fraction by the Dalitz-plot fit.

To estimate the contributions of the individual resonances to the total decay rate, the fit fractions,

$$\mathrm{FF}_r = \frac{\int |a_r e^{i\delta_r} \mathcal{A}_r|^2 dM^2_{K_S^0 \pi^\pm(\mathrm{RS})} dM^2_{\pi^+ \pi^-}}{\int |\sum_j a_j e^{i\delta_j} \mathcal{A}_j|^2 dM^2_{K_S^0 \pi^\pm(\mathrm{RS})} dM^2_{\pi^+ \pi^-}}, \quad (5)$$

are calculated from the fitted amplitudes and phases. The statistical uncertainties on the fit fractions are determined by propagating the uncertainties on the amplitudes and phases. This is done by generating 1000 random parameter sets of amplitudes and phases according to the full covariance matrix of the fit and taking the standard deviation of the distribution of the 1000 calculated fit fractions.

The results of the combined D^0 and $\bar{D}^0$ Dalitz-plot fit for the relative amplitudes and phases of the included intermediate resonances can be found in Table I, together with the corresponding fit fractions. Table II shows the results for the fitted masses and widths of the $K^*(892)^\pm$, $f_0(600)$, and σ_2 contributions. The values for the $K^*(892)^\pm$ agree with the world-average values [29] within 2 MeV/c^2. The mistag fraction obtained from the Dalitz-plot fit is $1 - T = (0.98 \pm 0.14)\%$. A reduced χ^2 of 7387/5082, calculated from the deviations between data and fit in each bin, supports the quality of our model. The largest discrepancy comes from the high statistics corner of the Dalitz plot populated by the Cabibbo-favored decays with $K^*(892)^\pm$ resonance. The three mass-squared projections are shown in Fig. 4. The results for the fit fractions are consistent with the measurements from previous experiments [7,8,30,32].

B. Measurement of *CP*-violation asymmetries

As described in Sec. I, D^* tagging is used to measure *CP*-violation effects in the Dalitz decay. Although equal numbers of D^0 and $\bar{D}^0$ mesons are produced in the CDF II detector, the efficiency for reconstructing soft pions from the D^* decays causes an instrumental asymmetry between the numbers of observed D^0 and $\bar{D}^0$ decays. This instrumental asymmetry is mainly due to the tilt of COT cells described in Sec. II, which causes positively and negatively charged particles to hit the cells at different angles. Since only relative differences between the D^0 and $\bar{D}^0$ Dalitz plots are studied, an absolute efficiency difference is expected not to bias the observed physics asymmetries. However, an instrumental asymmetry depending on the transverse momentum of the additional pion can lead to efficiency discrepancies that vary over the Dalitz plot and has to be taken into account to avoid biased results.

Figure 5 shows the observed asymmetry,

$$A = \frac{N_{D^{*+}} - N_{D^{*-}}}{N_{D^{*+}} + N_{D^{*-}}}, \quad (6)$$

between the number of D^{*+} (D^0) and D^{*-} ($\bar{D}^0$) candidates as a function of the transverse momentum of the pion from the $D^{*\pm}$ decay. The asymmetry is larger at low $p_T(\pi_{D^{*\pm}})$. This means that the efficiency for reconstructing a D^0 or a $\bar{D}^0$ may differ over the Dalitz plot. The effect is corrected by reweighting the $\bar{D}^0$ Dalitz plot according to

TABLE I. Combined D^0 and $\bar{D}^0$ Dalitz-plot-fit results for the relative amplitudes and phases of the included intermediate resonances, together with the fit fractions calculated from them. Because of interference effects between the various resonances the fit fractions are not constrained to add up exactly to 100%.

Resonance	a	δ [°]	Fit fractions [%]
$K^*(892)^\pm$	1.911 ± 0.012	132.1 ± 0.7	61.80 ± 0.31
$K_0^*(1430)^\pm$	2.093 ± 0.065	54.2 ± 1.9	6.25 ± 0.25
$K_2^*(1430)^\pm$	0.986 ± 0.034	308.6 ± 2.1	1.28 ± 0.08
$K^*(1410)^\pm$	1.092 ± 0.069	155.9 ± 2.8	1.07 ± 0.10
$\rho(770)$	1	0	18.85 ± 0.18
$\omega(782)$	0.038 ± 0.002	107.9 ± 2.3	0.46 ± 0.05
$f_0(980)$	0.476 ± 0.016	182.8 ± 1.3	4.91 ± 0.19
$f_2(1270)$	1.713 ± 0.048	329.9 ± 1.6	1.95 ± 0.10
$f_0(1370)$	0.342 ± 0.021	109.3 ± 3.1	0.57 ± 0.05
$\rho(1450)$	0.709 ± 0.043	8.7 ± 2.7	0.41 ± 0.04
$f_0(600)$	1.134 ± 0.041	201.0 ± 2.9	7.02 ± 0.30
σ_2	0.282 ± 0.023	16.2 ± 9.0	0.33 ± 0.04
$K^*(892)^\pm$(DCS)	0.137 ± 0.007	317.6 ± 2.8	0.32 ± 0.03
$K_0^*(1430)^\pm$(DCS)	0.439 ± 0.035	156.1 ± 4.9	0.28 ± 0.04
$K_2^*(1430)^\pm$(DCS)	0.291 ± 0.034	213.5 ± 6.1	0.11 ± 0.03
Nonresonant	1.797 ± 0.147	94.0 ± 5.3	1.64 ± 0.27
Sum			107.25 ± 0.65

the deviations between the $p_T(\pi_{D^{*\pm}})$ distributions for positive and negative pion charges found in data.

Two different parametrization approaches to measure *CP*-violation asymmetries in a simultaneous Dalitz-plot fit to the D^0 and reweighted $\bar{D}^0$ samples are applied. The first one corresponds to an independent parametrization of the relative amplitudes and phases in the Dalitz-plot fits of the D^0 and $\bar{D}^0$ samples, respectively. Differences in the estimated resonance parameters can then be interpreted as *CP*-violation effects. The second parametrization approach is a simultaneous fit to the D^0 and $\bar{D}^0$ samples, where two additional parameters, representing *CP*-violation amplitudes and phases, are introduced for each resonance.

1. Independent D^0 and $\bar{D}^0$ parametrizations

The fitting procedure described in Sec. VI A is repeated with separate parametrizations for the amplitudes and phases in the D^0 and $\bar{D}^0$ samples. By performing a simultaneous D^0 and $\bar{D}^0$ fit, common parameters are used for the Gaussian-constrained masses and widths of the included resonances, the nonresonant contribution, the $K^*(892)^\pm$, $f_0(600)$, and σ_2 masses and widths, as well as the mistag fraction.

TABLE II. Combined D^0 and $\bar{D}^0$ Dalitz-plot-fit results for the masses and widths of the $K^*(892)^\pm$, $f_0(600)$, and σ_2 contributions.

Resonance	Mass [MeV/c^2]	Natural width [MeV/c^2]
$K^*(892)^\pm$	893.9 ± 0.1	51.9 ± 0.2
$f_0(600)$	527.3 ± 5.2	308.7 ± 8.9
σ_2	1150.5 ± 7.7	138.8 ± 7.8

To quantify possible *CP*-violation effects, the fit-fraction asymmetries,

$$A_{\mathrm{FF}} = \frac{\mathrm{FF}_{D^0} - \mathrm{FF}_{\bar{D}^0}}{\mathrm{FF}_{D^0} + \mathrm{FF}_{\bar{D}^0}}, \quad (7)$$

are calculated for each intermediate resonance, where the statistical uncertainties are determined by Gaussian uncertainties propagated from the statistical uncertainties of the individual fit fractions.

A measure for the overall integrated *CP* asymmetry is given by

$$A_{CP} = \frac{\int \frac{|\mathcal{M}|^2 - |\bar{\mathcal{M}}|^2}{|\mathcal{M}|^2 + |\bar{\mathcal{M}}|^2} dM^2_{K_S^0 \pi^\pm (\mathrm{RS})} dM^2_{\pi^+ \pi^-}}{\int dM^2_{K_S^0 \pi^\pm (\mathrm{RS})} dM^2_{\pi^+ \pi^-}}, \quad (8)$$

where $\mathcal{M}$ is the matrix element of Eq. (3) for the D^0 decay and $\bar{\mathcal{M}}$ the one for the $\bar{D}^0$ decay. The statistical uncertainty on A_{CP} is determined with the same procedure used for the determination of the fit-fraction uncertainties.

2. *CP*-violation amplitudes and phases

Following Ref. [6], a simultaneous fit to the D^0 and $\bar{D}^0$ samples is performed, where the matrix elements for D^0 and $\bar{D}^0$ read

$$\mathcal{M} = a_0 e^{i\delta_0} + \sum_j a_j e^{i(\delta_j + \phi_j)} \left(1 + \frac{b_j}{a_j}\right) \mathcal{A}_j,$$

$$\bar{\mathcal{M}} = a_0 e^{i\delta_0} + \sum_j a_j e^{i(\delta_j - \phi_j)} \left(1 - \frac{b_j}{a_j}\right) \mathcal{A}_j. \quad (9)$$

Compared to Eq. (3) the additional parameters b_j and ϕ_j, representing *CP*-violation amplitudes and phases, are
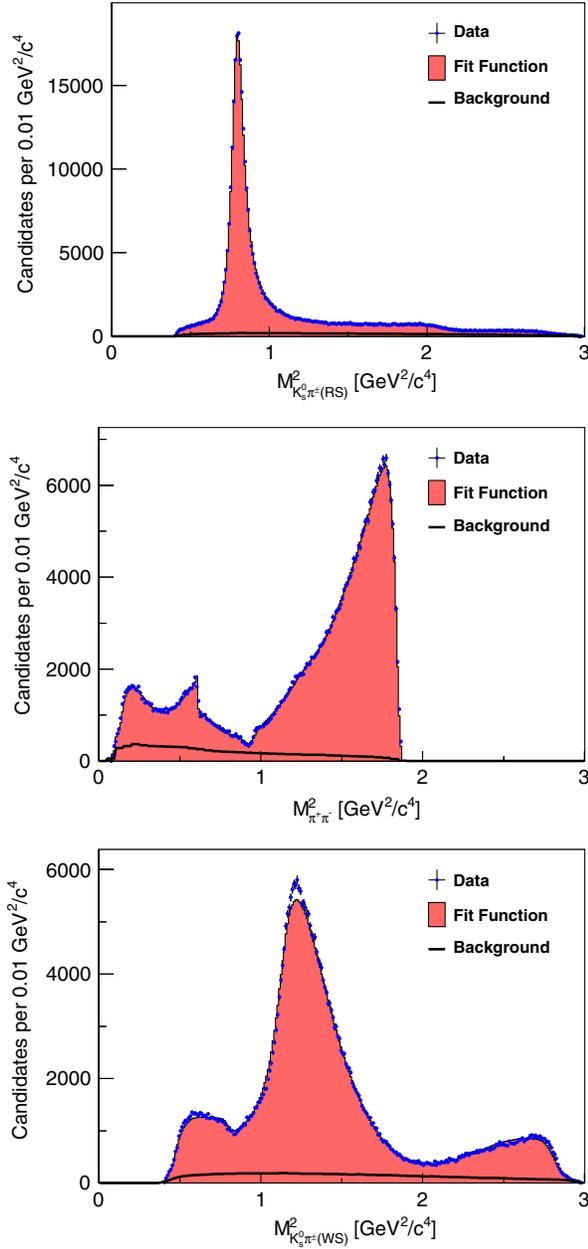
FIG. 4 (color online). Projections of the Dalitz-plot fit on the individual two-body masses, together with the corresponding distributions in data.

FIG. 5 (color online). Asymmetry between the numbers of reconstructed D^{*+} and D^{*-} candidates as a function of the soft pion's p_T.

$\bar{D}^0$ samples, and the applied efficiency distribution which is estimated by simulated events and may not adequately model the composition of trigger configurations in data. Modeling uncertainties arise from the chosen values for the radius parameters in the Blatt-Weisskopf form factors and the limited knowledge on the complex dynamics of the three-body decay. In this context, the stability of the determined CP-violation quantities under variations of the employed Dalitz model is tested. The contributions from the various sources to the total systematic uncertainties can be found in Tables III, IV, V, and VI.

A. Efficiency asymmetry

The reweighting procedure of the $\bar{D}^0$ Dalitz plot according to the deviations between the $p_T(\pi_{D^{*\pm}})$ distributions for positively and negatively charged pions may not fully correct for residual small asymmetries between the D^0 and $\bar{D}^0$ efficiency distributions. To estimate the size of a systematic effect originating from such an asymmetry, the Dalitz-plot fits are repeated without reweighting the $\bar{D}^0$ Dalitz plot. The scale of systematic uncertainties is estimated as the differences between the resulting values and the ones from the default fits.

B. Background asymmetry

To investigate a possible systematic effect originating from different Dalitz-plot distributions of the background in D^0 and $\bar{D}^0$ data, the Dalitz-plot fits are repeated with two independent background samples distinguished by the charge of the slow pion in the $D^{*\pm}$ decay. The systematic uncertainties are calculated as differences between the resulting values and the ones from the default fits.

C. Fit model

The systematic uncertainties originating from the specific model used for the Dalitz-plot fit are estimated by repeating the fits when one of the resonances $K^*(1410)^{\pm}$,

introduced. Again, common parameters are used for the Gaussian-constrained masses and widths of the included resonances, the nonresonant contribution, the $K^*(892)^{\pm}$, $f_0(600)$, and σ_2 masses and widths, as well as the mistag fraction.

VII. SYSTEMATIC UNCERTAINTIES

The systematic uncertainties are categorized into experimental and modeling uncertainties. The considered experimental sources are efficiency asymmetries varying over the Dalitz plot, asymmetries of the background in the D^0 and
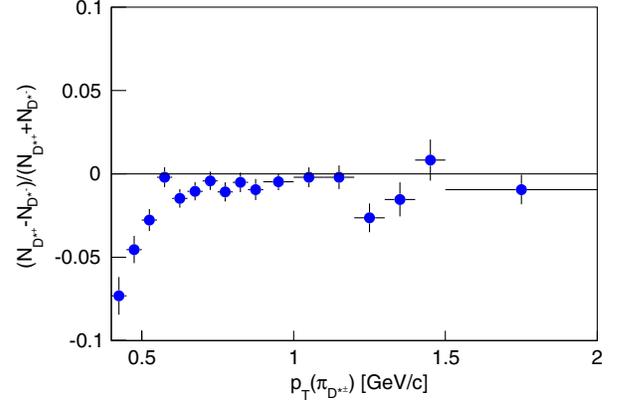
TABLE III. Systematic uncertainties on the fit-fraction asymmetry A_{FF} for each included intermediate resonance. The contributions from the efficiency asymmetry, the background asymmetry, the fit model, the trigger efficiency, and the Blatt-Weisskopf form factors are described in Sec. VII. The small values for the $\rho(770)$ resonance are due to the fixing of its parameters in the fit. The total systematic uncertainties are given by adding up the various contributions in quadrature. The corresponding statistical uncertainties are listed for comparison.

A_{FF} $[10^{-2}]$	Efficiency	Background	Fit model	Trigger	Form factors	Total uncertainties Systematic	Statistical
$K^*(892)^\pm$	0.09	0.13	0.27	0.09	0.23	0.40	0.33
$K_0^*(1430)^\pm$	0.9	0.5	3.2	1.1	1.3	3.8	2.4
$K_2^*(1430)^\pm$	0.8	0.3	3.9	0.1	0.6	4.1	4.0
$K^*(1410)^\pm$	0.4	1.0	6.2	0.6	0.9	6.4	5.7
$\rho(770)$	0.05	0.00	0.05	0.00	0.04	0.08	0.50
$\omega(782)$	0.6	0.3	1.1	1.0	2.0	2.6	6.0
$f_0(980)$	0.9	1.1	0.8	0.1	0.4	1.6	2.2
$f_2(1270)$	1.0	1.4	1.0	1.5	1.8	3.0	3.4
$f_0(1370)$	0.8	0.4	6.4	0.4	4.1	7.7	4.6
$\rho(1450)$	0.6	0.9	4.7	6.2	1.9	8.1	5.2
$f_0(600)$	0.2	0.2	2.9	0.2	2.1	3.6	2.7
σ_2	0.9	1.9	2.5	0.5	1.9	3.8	7.6
$K^*(892)^\pm$(DCS)	0.3	0.6	1.3	0.1	1.5	2.1	5.7
$K_0^*(1430)^\pm$(DCS)	0	0	5	8	5	10	11
$K_2^*(1430)^\pm$(DCS)	0	1	14	1	26	29	14

$f_0(1370)$, σ_2, $K_2^*(1430)^\pm$(DCS), or the nonresonant contribution is excluded from the model. These are the least significant contributions, or in the case of σ_2, because of the controversy over the existence of such a state. For each case, the resulting CP-violation quantities are compared to the values from the default fits and the largest deviations are used as modeling systematic uncertainties.

D. Efficiency model

As described in Sec. II, different trigger configurations with thresholds of 4, 5.5, and 6.5 GeV/c on the scalar sum of the transverse momenta of the two trigger tracks are applied for the on-line event selection. The simulated events, used to determine the reconstruction efficiency across the Dalitz plot, are required to pass the different trigger configurations in the same proportions as the actual data. Any mismodeling of the efficiency is expected to cancel between D^0 and $\bar{D}^0$ candidates, to first order. To estimate residual higher-order effects, an efficiency determined with simulated events satisfying the 6.5 GeV/c trigger threshold is used, and the difference with the default efficiency is taken as a systematic uncertainty.

TABLE IV. Systematic uncertainties on the CP-violation amplitude b for each included intermediate resonance. Further explanations can be found in the caption of Table III.

b	Efficiency	Background	Fit model	Trigger	Form factors	Total uncertainties Systematic	Statistical
$K^*(892)^\pm$	0.011	0.001	0.000	0.001	0.002	0.011	0.004
$K_0^*(1430)^\pm$	0.022	0.009	0.029	0.009	0.015	0.041	0.028
$K_2^*(1430)^\pm$	0.003	0.004	0.022	0.003	0.001	0.023	0.024
$K^*(1410)^\pm$	0.006	0.000	0.015	0.011	0.007	0.021	0.037
$\rho(770)$	0.007	0.003	0.003	0.001	0.001	0.008	0.006
$\omega(782)$	0.000	0.000	0.000	0.000	0.000	0.000	0.002
$f_0(980)$	0.002	0.003	0.001	0.000	0.001	0.004	0.005
$f_2(1270)$	0.003	0.008	0.008	0.003	0.005	0.013	0.037
$f_0(1370)$	0.002	0.005	0.008	0.008	0.017	0.021	0.008
$\rho(1450)$	0.016	0.023	0.107	0.071	0.032	0.135	0.022
$f_0(600)$	0.011	0.001	0.018	0.002	0.013	0.025	0.017
σ_2	0.002	0.002	0.002	0.001	0.001	0.004	0.012
$K^*(892)^\pm$(DCS)	0.001	0.001	0.001	0.000	0.001	0.002	0.005
$K_0^*(1430)^\pm$(DCS)	0.003	0.005	0.030	0.008	0.015	0.035	0.024
$K_2^*(1430)^\pm$(DCS)	0.005	0.001	0.006	0.002	0.015	0.017	0.029

TABLE V.   Systematic uncertainties on the *CP*-violation phase ϕ for each included intermediate resonance. Further explanations can be found in the caption of Table III.

ϕ [°]	Efficiency	Background	Fit model	Trigger	Form factors	Total uncertainties Systematic	Statistical
$K^*(892)^\pm$	0.0	0.1	1.0	0.2	0.8	1.3	1.4
$K_0^*(1430)^\pm$	0.0	0.0	2.1	0.2	0.7	2.2	1.7
$K_2^*(1430)^\pm$	0.1	0.2	1.0	0.3	0.4	1.1	1.8
$K^*(1410)^\pm$	0.1	0.0	0.8	1.3	1.6	2.2	1.9
$\rho(770)$	0.1	0.3	1.1	0.2	0.8	1.4	1.5
$\omega(782)$	0.3	0.6	0.9	0.1	0.8	1.4	2.2
$f_0(980)$	0.2	0.0	0.8	0.0	0.7	1.1	1.3
$f_2(1270)$	0.2	0.2	1.3	0.7	1.4	2.1	1.9
$f_0(1370)$	1.0	1.2	1.9	1.0	0.9	2.8	1.7
$\rho(1450)$	0.0	0.6	2.0	3.1	1.2	3.9	1.7
$f_0(600)$	0.1	0.2	1.3	0.2	0.3	1.4	1.5
σ_2	0.2	0.3	0.7	0.4	0.7	1.1	2.9
$K^*(892)^\pm$(DCS)	0.1	0.5	1.1	0.1	0.1	1.2	2.3
$K_0^*(1430)^\pm$(DCS)	0.0	0.3	3.5	1.0	1.3	3.9	4.0
$K_2^*(1430)^\pm$(DCS)	0.6	0.5	2.3	0.5	1.7	3.0	5.3

E. Blatt-Weisskopf form factors

In the default Dalitz-plot fits, the chosen values for the radius parameter R in the Blatt-Weisskopf form factors are $R = 5 \ (\text{GeV}/c)^{-1}$ for the D^0 and $R = 1.5 \ (\text{GeV}/c)^{-1}$ for all intermediate resonances [26]. To estimate the systematic uncertainties originating from deviations from these values, the Dalitz-plot fits are repeated with both values for the radius parameter halved and doubled. The systematic uncertainties are then calculated as the largest differences between the resulting values and the ones from the default fits.

F. Further checks

To assess the robustness of the fitting procedure, the following checks were done, each leading to results that agree with the default fits within the expected variations.

To test the effects of the Dalitz-plot binning the fits are repeated when varying the bin widths from 0.025 to 0.03 and 0.05 GeV^2/c^4.

Discrepancies between data and the Dalitz-plot fit are visible in Fig. 4, in particular, at the peak of the $K^*(892)^\pm$ signal. To verify the results, the fits are repeated when

excluding the Dalitz-plot regions with the largest discrepancies between the fit values and data.

Instead of using Gaussian constraints, the masses and decay widths of the included resonances are fixed to the values in Ref. [28] for $f_0(980)$ and $f_0(1370)$, and to the world-average values [29] for the others, except for $K^*(892)^\pm$, $f_0(600)$, and σ_2 which are still unconstrained parameters in the fit.

The Dalitz-plot fits are repeated with an alternative background model, where the combinatorial background and the combinations of true D^0 candidates with a random pion are modeled by D^{*+} sidebands and the distribution of misreconstructed D^0 candidates is modeled by means of an inclusive charm simulated data set. The ratio of combinatorial background and combinations of true D^0 candidates with a random pion is assumed to be independent of the D^{*+} mass difference distribution. Since this assumption is not completely valid, especially close to the kinematic threshold, the method is only chosen as a check of the default background model described in Sec. VI A.

VIII. RESULTS

All *CP*-violation quantities are found to be consistent with zero. The results for the *CP*-violation amplitudes and phases, defined in Eq. (9) and obtained from the simultaneous fit to the D^0 and $\bar{D}^0$ Dalitz plots, are displayed in Table VII. The fit-fraction asymmetries for the intermediate resonances, defined in Eq. (7), are listed in Table VIII. The overall time-integrated *CP* asymmetry, defined in Eq. (8), is determined to be

$$A_{CP} = (-0.05 \pm 0.57(\text{stat}) \pm 0.54(\text{syst}))\%. \qquad (10)$$

This value includes the contribution from time-integrated *CP* violation in the mixing of the involved K^0 mesons. We

TABLE VI.   Systematic uncertainties on the overall integrated *CP* asymmetry. Further explanations can be found in the caption of Table III.

Effect	Uncertainty on A_{CP} [10^{-2}]
Efficiency	0.36
Background	0.09
Fit model	0.37
Trigger	0.05
Form factors	0.10
Total systematic	0.54
Statistical	0.57

TABLE VII. Results of the simultaneous D^0-$\bar{D}^0$ Dalitz-plot fit for the *CP*-violation amplitudes, b, and phases, ϕ. The first uncertainties are statistical and the second systematic.

Resonance	b	ϕ [°]
$K^*(892)^\pm$	$+0.004 \pm 0.004 \pm 0.011$	$-0.8 \pm 1.4 \pm 1.3$
$K_0^*(1430)^\pm$	$+0.044 \pm 0.028 \pm 0.041$	$-1.8 \pm 1.7 \pm 2.2$
$K_2^*(1430)^\pm$	$+0.018 \pm 0.024 \pm 0.023$	$-1.1 \pm 1.8 \pm 1.1$
$K^*(1410)^\pm$	$-0.010 \pm 0.037 \pm 0.021$	$-1.6 \pm 1.9 \pm 2.2$
$\rho(770)$	$-0.003 \pm 0.006 \pm 0.008$	$-0.5 \pm 1.5 \pm 1.4$
$\omega(782)$	$-0.003 \pm 0.002 \pm 0.000$	$-1.8 \pm 2.2 \pm 1.4$
$f_0(980)$	$-0.001 \pm 0.005 \pm 0.004$	$-0.1 \pm 1.3 \pm 1.1$
$f_2(1270)$	$-0.035 \pm 0.037 \pm 0.013$	$-2.0 \pm 1.9 \pm 2.1$
$f_0(1370)$	$-0.002 \pm 0.008 \pm 0.021$	$-0.1 \pm 1.7 \pm 2.8$
$\rho(1450)$	$-0.016 \pm 0.022 \pm 0.135$	$-1.7 \pm 1.7 \pm 3.9$
$f_0(600)$	$-0.012 \pm 0.017 \pm 0.025$	$-0.3 \pm 1.5 \pm 1.4$
σ_2	$-0.011 \pm 0.012 \pm 0.004$	$-0.2 \pm 2.9 \pm 1.1$
$K^*(892)^\pm$(DCS)	$+0.001 \pm 0.005 \pm 0.002$	$-3.8 \pm 2.3 \pm 1.2$
$K_0^*(1430)^\pm$(DCS)	$+0.022 \pm 0.024 \pm 0.035$	$-3.3 \pm 4.0 \pm 3.9$
$K_2^*(1430)^\pm$(DCS)	$-0.018 \pm 0.029 \pm 0.017$	$+4.2 \pm 5.3 \pm 3.0$

determine this contribution with the method described in Ref. [33] to be -0.07%, much smaller than the A_{CP} measurement uncertainty.

A. Indirect *CP* violation

Following the procedure described in Ref. [16], it is possible to disentangle indirect from direct *CP*-violation effects by means of the D^0 decay time distribution. The direct and indirect *CP* asymmetries are related to the time-integrated asymmetry by

$$A_{CP} = A_{CP}^{\mathrm{dir}} + \frac{\langle t \rangle}{\tau} A_{CP}^{\mathrm{ind}}, \qquad (11)$$

where τ is the mean D^0 lifetime. The mean observed decay time $\langle t \rangle$ is determined from the background subtracted D^0 decay time distribution. We correct for the fraction of nonprompt events that is estimated from the D^{*+} impact

parameter significance distribution, and obtain a mean observed decay time of $\langle t \rangle = (2.28 \pm 0.03)\tau(D^0)$. To compare with the recent CDF measurement of *CP*-violation asymmetries in $D^0 \to \pi^+\pi^-$ and $D^0 \to K^+K^-$ decays, $A_{CP}^{\mathrm{ind}}(D^0 \to h^+h^-) = (-0.01 \pm 0.06(\mathrm{stat}) \pm 0.04(\mathrm{syst}))\%$ [16], we determine the indirect *CP* asymmetry for the case of no direct *CP* violation to be

$$A_{CP}^{\mathrm{ind}} = (-0.02 \pm 0.25(\mathrm{stat}) \pm 0.24(\mathrm{syst}))\%. \qquad (12)$$

B. Individual *CP*-violation asymmetries

The CLEO experiment also quotes *CP*-violation quantities called interference fractions (IF) and individual *CP* asymmetries, A_{CP}, in each subresonance [6]. These are defined as $A_{CP_j} = \frac{\mathrm{IF}_j}{\mathrm{FF}_j}$, where

$$\mathrm{IF}_j = \frac{|\int \sum_k (2a_k e^{i\delta_k} \sin(\phi_k + \phi_j)\mathcal{A}_k)b_j \mathcal{A}_j dM^2_{K_S^0 \pi^\pm(\mathrm{RS})} dM^2_{\pi^+\pi^-}|}{(\int |\mathcal{M}|^2 dM^2_{K_S^0 \pi^\pm(\mathrm{RS})} dM^2_{\pi^+\pi^-} + \int |\bar{\mathcal{M}}|^2 dM^2_{K_S^0 \pi^\pm(\mathrm{RS})} dM^2_{\pi^+\pi^-})}. \qquad (13)$$

Since these values are positive by construction, only upper limits are given. The calculation is performed with the same method used for the determination of the fit fractions, where the 90% and 95% quantiles of resulting distributions are used as the corresponding C.L. upper limits. To account for systematic uncertainties for each resonance, the largest values of all fits with the different systematic variations are taken. The resulting 90% and 95% C.L. on the individual *CP* asymmetries are listed in Table IX.

IX. MODEL-INDEPENDENT APPROACH

Following Ref. [10], a model-independent search for *CP* violation in the Dalitz-plot distribution of the decay

$D^0 \to K_S^0 \pi^+\pi^-$ is performed by comparing the binned Dalitz plots for D^0 and $\bar{D}^0$ meson decays. No assumptions about the resonant substructure of the decay are used. The approach serves as a complementary verification of the results from the Dalitz-plot fits described in the previous sections. However, this method only detects the presence of a significant *CP*-violation effect, without allowing a determination of the size of the asymmetries.

The signed significance of the asymmetry between the numbers of D^0 and $\bar{D}^0$ candidates, $(N_{D^0} - N_{\bar{D}^0})/\sqrt{N_{D^0} + N_{\bar{D}^0}}$, is calculated for each bin and studied as a function of the squared $K_S^0 \pi^\pm$ and $\pi^+\pi^-$ masses. In this calculation the number of $\bar{D}^0$ events is normalized to the

TABLE VIII. Fit-fraction asymmetries, A_{FF}, for the included intermediate resonances. The first uncertainties are statistical and the second systematic.

Resonance	A_{FF} [%]
$K^*(892)^\pm$	$+0.36 \pm 0.33 \pm 0.40$
$K_0^*(1430)^\pm$	$+4.0 \pm 2.4 \pm 3.8$
$K_2^*(1430)^\pm$	$+2.9 \pm 4.0 \pm 4.1$
$K^*(1410)^\pm$	$-2.3 \pm 5.7 \pm 6.4$
$\rho(770)$	$-0.05 \pm 0.50 \pm 0.08$
$\omega(782)$	$-12.6 \pm 6.0 \pm 2.6$
$f_0(980)$	$-0.4 \pm 2.2 \pm 1.6$
$f_2(1270)$	$-4.0 \pm 3.4 \pm 3.0$
$f_0(1370)$	$-0.5 \pm 4.6 \pm 7.7$
$\rho(1450)$	$-4.1 \pm 5.2 \pm 8.1$
$f_0(600)$	$-2.7 \pm 2.7 \pm 3.6$
σ_2	$-6.8 \pm 7.6 \pm 3.8$
$K^*(892)^\pm$(DCS)	$+1.0 \pm 5.7 \pm 2.1$
$K_0^*(1430)^\pm$(DCS)	$+12 \pm 11 \pm 10$
$K_2^*(1430)^\pm$(DCS)	$-10 \pm 14 \pm 29$

one of D^0. Possible *CP*-violation asymmetries would appear as clusters of same-sign discrepancies. The sum of the squares of the significance asymmetries in each bin is expected to follow a χ^2 distribution. The *p* value can be calculated considering the number of degrees of freedom equal to the number of Dalitz-plot bins minus one (for the normalization). Furthermore, one expects a Gaussian distribution with mean equal to 0 and width of 1 for the histogram of the asymmetry significance distribution in case of vanishing *CP* violation.

The method is verified in simulation and then applied to data. As we test relative differences between D^0 and $\bar{D}^0$ at different places in the Dalitz plot, we normalize D^0 and $\bar{D}^0$ to the same area. With this approach, all asymmetries that are uniformly distributed over the Dalitz plot completely cancel.

TABLE IX. Upper limits for individual *CP*-violation asymmetries.

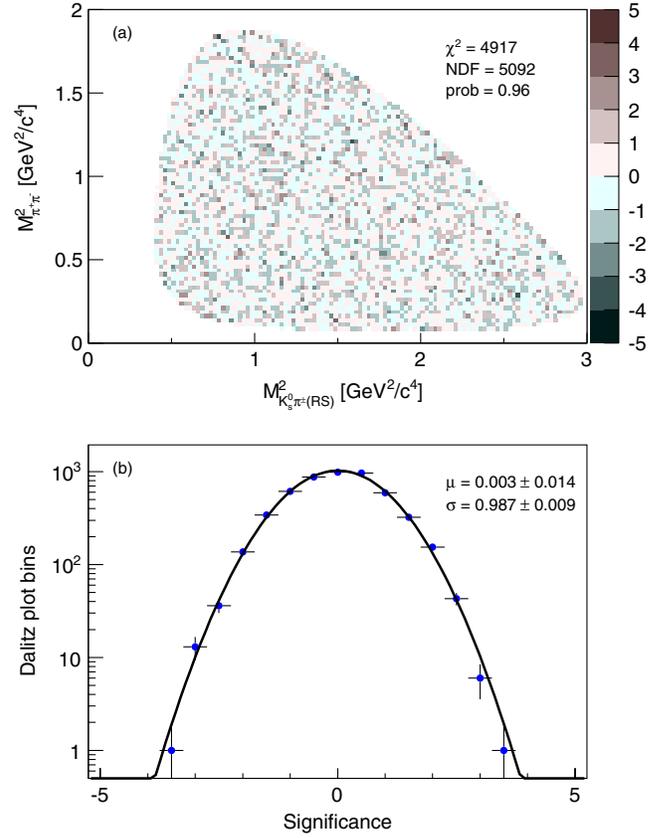| Resonance	A_{CP} [%] (90% C.L.)	A_{CP} [%] (95% C.L.)
$K^*(892)^\pm$	0.014	0.018
$K_0^*(1430)^\pm$	0.80	1.2
$K_2^*(1430)^\pm$	0.45	0.62
$K^*(1410)^\pm$	6.6	8.4
$\rho(770)$	0.038	0.051
$\omega(782)$	0.51	0.66
$f_0(980)$	0.13	0.17
$f_2(1270)$	1.6	2.1
$f_0(1370)$	25	37
$\rho^0(1450)$	6.5	8.2
$f_0(600)$	0.17	0.24
σ_2	3.1	3.9
$K^*(892)^\pm$(DCS)	1.7	2.3
$K_0^*(1430)^\pm$(DCS)	22	28
$K_2^*(1430)^\pm$(DCS)	12	16

FIG. 6 (color online). Distribution of the asymmetry significance (a) as a function of the squared $K_S^0\pi^\pm$ and $\pi^+\pi^-$ masses and (b) as a histogram.

However, an efficiency asymmetry varying over the Dalitz plot may mimic *CP* violation. As described in Sec. VI B, this problem is also relevant for the Dalitz-plot fits, and the reweighting procedure used there is applied here as well.

The resulting Dalitz-plot distribution of the asymmetry significance between the numbers of D^0 and $\bar{D}^0$ candidates, with bin widths of 0.025 GeV$^2/c^4$ in both dimensions, and the corresponding histogram are shown in Fig. 6. The parameters obtained from the fit, $\mu = 0.003 \pm 0.014$ and $\sigma = 0.987 \pm 0.009$, are consistent with a Gaussian distribution centered at zero with unit variance, and the *p* value calculated from the asymmetry significance distribution is $p = 0.96$. The model-independent approach confirms that no *CP* violation is observed between the D^0 and $\bar{D}^0$ decay amplitudes into the $K_S^0\pi^+\pi^-$ final state.

X. CONCLUSION

A Dalitz-amplitude analysis is employed to study the resonant substructure of the $D^0 \rightarrow K_S^0\pi^+\pi^-$ three-body decay. In performing a full Dalitz-plot fit, the relative amplitudes, phases, and fit fractions of the various intermediate resonances are determined. The results are compatible and comparable in precision to the measurements from previous experiments [7,8,30,32].

In simultaneous fits to the D^0 and $\bar{D}^0$ Dalitz plots, a *CP*-violation fit fraction, amplitude, and phase are determined for each included intermediate resonance. None of these is significantly different from zero. This also holds for the overall integrated *CP* asymmetry, $A_{CP} = (-0.05 \pm 0.57(\text{stat}) \pm 0.54(\text{syst}))\%$. A complementary model-independent search for localized *CP*-violation differences in relative Dalitz-plot densities between the binned D^0 and $\bar{D}^0$ distributions yields a result consistent with zero, too. In conclusion, the most precise values for the overall integrated *CP* asymmetry as well as the *CP*-violation fit fractions, amplitudes, and phases are reported; no indications for any *CP*-violation effects in $D^0 \to K_S^0 \pi^+ \pi^-$ decays are found, in agreement with the standard model.

ACKNOWLEDGMENTS

[1] M. Kobayashi and T. Maskawa, Prog. Theor. Phys. **49**, 652 (1973).

[2] R. Aaij *et al.* (LHCb Collaboration), Phys. Rev. Lett. **108**, 111602 (2012).

[3] T. Aaltonen *et al.* (CDF Collaboration), arXiv:1207.2158.

[4] I. I. Bigi and H. Yamamoto, Phys. Lett. B **349**, 363 (1995).

[5] Z.-Z. Xing, Phys. Lett. B **353**, 313 (1995).

[6] D. M. Asner *et al.* (CLEO Collaboration), Phys. Rev. D **70**, 091101 (2004).

[7] L. M. Zhang *et al.* (Belle Collaboration), Phys. Rev. Lett. **99**, 131803 (2007).

[8] P. del Amo Sanchez *et al.* (*BABAR* Collaboration), Phys. Rev. Lett. **105**, 081803 (2010).

[9] D. Asner *et al.* (The Heavy Flavor Averaging Group), arXiv:1010.1589v2.

[10] I. Bediaga, I. I. Bigi, A. Gomes, G. Guerrer, J. Miranda, and A. C. dos Reis, Phys. Rev. D **80**, 096006 (2009).

[11] D. Acosta *et al.* (CDF Collaboration), Phys. Rev. D **71**, 032001 (2005).

[12] A. Sill, Nucl. Instrum. Methods Phys. Res., Sect. A **447**, 1 (2000).

[13] A. Affolder *et al.*, Nucl. Instrum. Methods Phys. Res., Sect. A **453**, 84 (2000).

[14] C. S. Hill, Nucl. Instrum. Methods Phys. Res., Sect. A **530**, 1 (2004).

[15] A. Affolder *et al.*, Nucl. Instrum. Methods Phys. Res., Sect. A **526**, 249 (2004).

[16] T. Aaltonen *et al.* (CDF Collaboration), Phys. Rev. D **85**, 012009 (2012).

[17] E. J. Thomson *et al.*, IEEE Trans. Nucl. Sci. **49**, 1063 (2002).

[18] W. Ashmanskas *et al.*, Nucl. Instrum. Methods Phys. Res., Sect. A **518**, 532 (2004); L. Ristori and G. Punzi, Annu. Rev. Nucl. Part. Sci. **60**, 595 (2010).

[19] F. Wick, Ph.D. thesis, Karlsruhe Institute of Technology, 2011.

[20] M. Feindt and U. Kerzel, Nucl. Instrum. Methods Phys. Res., Sect. A **559**, 190 (2006).

[21] M. Pivk and F. R. Le Diberder, Nucl. Instrum. Methods Phys. Res., Sect. A **555**, 356 (2005).

[22] T. Aaltonen *et al.* (CDF Collaboration), Phys. Rev. D **84**, 012003 (2011).

[23] R. H. Dalitz, Philos. Mag. **44**, 1068 (1953).

[24] D. J. Herndon, P. Söding, and R. J. Cashmore, Phys. Rev. D **11**, 3165 (1975).

[25] D. J. Herndon, P. Söding, and R. J. Cashmore, Phys. Rev. D **5**, 624 (1972).

[26] S. Kopp *et al.* (CLEO Collaboration), Phys. Rev. D **63**, 092001 (2001).

[27] G. J. Gounaris and J. J. Sakurai, Phys. Rev. Lett. **21**, 244 (1968).

[28] E. M. Aitala *et al.* (E791 Collaboration), Phys. Rev. Lett. **86**, 765 (2001).

[29] K. Nakamura *et al.* (Particle Data Group), J. Phys. G **37**, 075021 (2010).

[30] A. Poluektov *et al.* (Belle Collaboration), Phys. Rev. D **70**, 072003 (2004).

[31] D. J. Lange, Nucl. Instrum. Methods Phys. Res., Sect. A **462**, 152 (2001).

[32] H. Muramatsu *et al.* (CLEO Collaboration), Phys. Rev. Lett. **89**, 251802 (2002).

[33] Y. Grossman and Y. Nir, J. High Energy Phys. 04 (2012) 002.